Block Copolymer Self-Assembly–Directed Single-Crystal Homo- and Heteroepitaxial Nanostructures

Hitesh Arora *et al.*

Science **330**, 214 (2010);
DOI: 10.1126/science.1193369

Science (print ISSN 0036-8075; online ISSN 1095-9203) is published weekly, except the last week in December, by the American Association for the Advancement of Science, 1200 New York Avenue NW, Washington, DC 20005.

tially nonuniform systems when highly stressed regions are encountered; however, we do not yet fully understand what causes rupture nucleation in our system. We find that nucleation locations are often regions where $\tau(x)/\sigma(x)$ is maximal (for instance, see Fig. 2C). Hence, either low $\sigma(x)$ or high $\tau(x)$ can influence the location and initiation of rupture fronts. Increased $\sigma(x)$, as at the leading edge in Fig. 2F, will serve to suppress nucleation. Likewise, values of $\tau(x)$ that oppose the applied shear, such as at the trailing edges of Fig. 2, will have the same effect. The high values of both $\sigma(x)$ and $\tau(x)$ associated with corners can either make edges susceptible to rupture nucleation (Fig. 2A) or suppress rupture, depending on the competition between them.

Once a rupture front is nucleated, knowledge of the local stress profiles along the interface allows us to predict the rupture mode and could indicate when a rapid mode will either arrest to a complete stop (Fig. 2A) or evolve into a slow front (Fig. 2B). Thus, the initiation/transition locations of the slow fronts observed in previous studies (*5*, *6*) become clearer. Such questions of predictability are important when applied to understanding earthquake dynamics (*3*). Although $\tau(x)/\sigma(x)$ is an elusive quantity to measure along natural faults, indirect measurements may be possible by coupling precise measurements of spatial variations of V(x) to laboratory measurements of the $\tau(x)/\sigma(x)$ dependence on V, as in Fig. 3. This estimate of this otherwise inaccessible quantity could provide some measure of predictability of the eventual size and dynamics of fast earthquakes along natural faults.

References and Notes

1. F. P. Bowden, D. Tabor, *The Friction and Lubrication of Solids* (Oxford Univ. Press, New York, ed. 2, 2001).
2. S. Das, *Pure Appl. Geophys.* **160**, 579 (2003).
3. C. H. Scholz, *The Mechanics of Earthquakes and Faulting* (Cambridge Univ. Press, Cambridge, ed. 2, 2002).
4. Y. Ben-Zion, *Rev. Geophys.* **46**, RG4006 (2008).
5. S. M. Rubinstein, G. Cohen, J. Fineberg, *Nature* **430**, 1005 (2004).
6. S. M. Rubinstein, G. Cohen, J. Fineberg, *Phys. Rev. Lett.* **98**, 226103 (2007).
7. M. Ohnaka, L. F. Shen, *J. Geophys. Res. Solid Earth* **104**, 817 (1999).
8. S. Nielsen, J. Taddeucci, S. Vinciguerra, *Geophys. J. Int.* **180**, 697 (2010).
9. P. G. Okubo, J. H. Dieterich, *J. Geophys. Res. Solid Earth* **89**, 5817 (1984).
10. T. L. Johnson, C. H. Scholz, *J. Geophys. Res.* **81**, 881 (1976).
11. O. Ben-David, S. M. Rubinstein, J. Fineberg, *Nature* **463**, 76 (2010).
12. K. W. Xia, A. J. Rosakis, H. Kanamori, *Science* **303**, 1859 (2004).
13. S. Das, K. Aki, *Geophys. J. R. Astron. Soc.* **50**, 643 (1977).
14. R. Burridge, *Geophys. J. R. Astron. Soc.* **35**, 439 (1973).
15. R. Madariaga, K. B. Olsen, *Pure Appl. Geophys.* **157**, 1981 (2000).
16. D. J. Andrews, *J. Geophys. Res. Solid Earth* **81**, 5679 (1976).
17. O. M. Braun, I. Barel, M. Urbakh, *Phys. Rev. Lett.* **103**, 194301 (2009).
18. Y. J. Liu, J. R. Rice, *J. Geophys. Res. Solid Earth* **110**, B08307 (2005).
19. Y. Ito, K. Obara, K. Shiomi, S. Sekine, H. Hirose, *Science* **315**, 503 (2007); published online 30 November 2006 (10.1126/science.1134454).
20. A. T. Linde, M. T. Gladwin, M. J. S. Johnston, R. L. Gwyther, R. G. Bilham, *Nature* **383**, 65 (1996).
21. G. Rogers, H. Dragert, *Science* **300**, 1942 (2003); published online 8 May 2003 (10.1126/science.1084783).
22. R. J. Archuleta, *J. Geophys. Res. Solid Earth* **89**, 4559 (1984).
23. M. Bouchon, M. Vallée, *Science* **301**, 824 (2003).
24. Materials and methods are available as supporting material on *Science* Online.
25. S. M. Rubinstein, G. Cohen, J. Fineberg, *Phys. Rev. Lett.* **96**, 256103 (2006).
26. T. Baumberger, C. Caroli, *Adv. Phys.* **55**, 279 (2006).
27. L. B. Freund, *Dynamic Fracture Mechanics* (Cambridge Univ. Press, Cambridge, 1990).
28. E. M. Dunham, *J. Geophys. Res. Solid Earth* **112**, B07302 (2007).
29. Z. Q. Shi, Y. Ben-Zion, A. Needleman, *J. Mech. Phys. Solids* **56**, 5 (2008).

30. We thank E. Bouchbinder and A. Sagy for insightful comments and S. Kimhi for help with the system design. We acknowledge the support of grant 2006288 awarded by the U.S.-Israel Binational Science Foundation and the James S. McDonnell Foundation. We also acknowledge the European Science Foundation EUROCORES program FANAS for support via the Israel Science Foundation (grant 57/07). J.F. thanks the Max Born Chair for Natural Philosophy for support.

Supporting Online Material

www.sciencemag.org/cgi/content/full/330/6001/211/DC1
Materials and Methods
Fig. S1
References

7 July 2010; accepted 19 August 2010
10.1126/science.1194777

Block Copolymer Self-Assembly–Directed Single-Crystal Homo- and Heteroepitaxial Nanostructures

Hitesh Arora,[1,2]* Phong Du,[1]† Kwan W. Tan,[1] Jerome K. Hyun,[3]‡ John Grazul,[4] Huolin L. Xin,[3] David A. Muller,[5,6] Michael O. Thompson,[1] Ulrich Wiesner[1]§

Epitaxy is a widely used method to grow high-quality crystals. One of the key challenges in the field of inorganic solids is the development of epitaxial single-crystal nanostructures. We describe their formation from block copolymer self-assembly–directed nanoporous templates on single-crystal Si backfilled with Si or NiSi through a laser-induced transient melt process. Depending on thickness, template removal leaves either an array of nanopillars or porous nanostructures behind. For stoichiometric NiSi deposition, the template pores provide confinement, enabling heteroepitaxial growth. Irradiation through a mask provides access to hierarchically structured materials. These results on etchable and non-etchable materials suggest a general strategy for growing epitaxial single-crystal nanostructured thin films for fundamental studies and a wide variety of applications, including energy conversion and storage.

Most nanostructured inorganic materials directed by organic molecule self-assembly are either amorphous or polycrystalline (*1*–*7*). One of the key remaining issues in the field is the development of single-crystal nanostructured inorganic materials with an epitaxial relation to an underlying substrate. Such materials may enable advances in areas such as energy generation and storage. For example, the charge carrier mobility in crystalline materials in small dimensions is substantially reduced by grain boundaries, which decreases charge collection efficiency in photovoltaic cells (*8*). Although large-area patterned inorganic epitaxial single crystals have been synthesized before, the patterns have been limited to the micrometer scale (*9*). Several attempts have been made to achieve smaller-scale structures. Block copolymer thin films have been used as etching masks to generate inorganic nanostructures, but the process depends on etchable substrates, and the features can only be vertically aligned and are always open from the top (*10*–*13*). Laser-induced melting of Si and subsequent infiltration into a quartz mold have been previously described (*14*). The process relies on so-called top-down lithography and etching to make a mold, however, with a structural period of hundreds of nanometers. Moreover, the epitaxial relation of the resulting structures to the substrate was not elucidated, and the heteroepitaxy of non-etchable materials was not addressed. Directional rapid solidification and epitaxy have been described for semicrystalline block copolymer films, but without any inorganic materials (*15*). Hierarchically ordered oxide structures have been demonstrated before, but the oxides were not single-crystalline (*16*). Mesoporous, single-crystalline,

[1]Department of Materials Science and Engineering, Cornell University, Ithaca, NY 14853, USA. [2]School of Chemical and Biomolecular Engineering, Cornell University, Ithaca, NY 14853, USA. [3]Department of Physics, Cornell University, Ithaca, NY 14853, USA. [4]Cornell Center for Materials Research, Cornell University, Ithaca, NY 14853, USA. [5]School of Applied and Engineering Physics, Cornell University, Ithaca, NY 14853, USA. [6]Kavli Institute at Cornell for Nanoscale Science, Cornell University, Ithaca, NY 14853, USA.

*Present address: Intel Corporation, Chandler, AZ 85226, USA.
†Present address: DuPont Chemical Company, Wilmington, DE 19880, USA.
‡Present address: Department of Materials Science and Engineering, Northwestern University, Evanston, IL 60208, USA.
§To whom correspondence should be addressed. E-mail: ubw1@cornell.edu

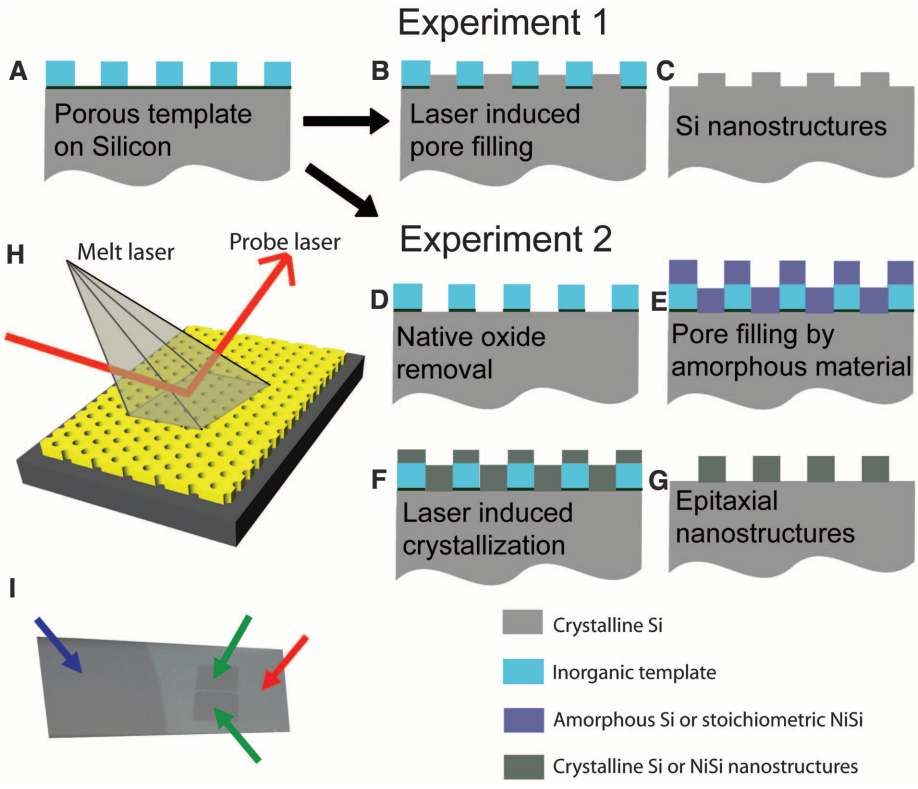

Fig. 1. Schematic of single-crystal homoepitaxial Si and heteroepitaxial NiSi nanostructure generation. (**A**) Porous template. (**B** and **C**) First experimental process. (**D** to **G**) Second experimental process. (**H**) Laser irradiation schematic. (**I**) Photograph of Si wafer with bare crystalline Si substrate (blue arrow), with a-Si deposited (red arrow) and spots after laser-induced crystallization (green arrows).

mixed transition-metal-oxide particles and calcite single crystals with gyroid morphology have been generated from surfactant and polymer self-assembly, respectively, but their epitaxial relations to substrates have not been described (*17*–*19*). Finally, epitaxial thin-film oxide growth on single-crystal substrates and subsequent topotactic crystal transformation with substantial volume shrinkage leading to pores with crystallographic alignment have recently been demonstrated. The process did not involve organic molecule self-assembly, however, and the topotactic transformation process is most likely materials-specific and thus may not easily be generalized to other materials (*20*).

In this work, we used nanoporous thin films ~15 to 100 nm thick on Si to define and control epitaxial crystallization of Si and NiSi, with templates having periodicities on the scale of tens of nanometers. Template thin films were obtained in a bottom-up self-assembly approach using inorganic precursors, a process directed by block copolymer self-assembly. Template pores were filled with amorphous Si or NiSi (a-Si or a-NiSi). Subsequently, laser-induced melting converted the amorphous phase into crystalline materials. Depending on template thickness, either arrays of isolated nanopillars or interconnected three-dimensional nanostructures were generated.

The processes we used are schematically shown in Fig. 1, A to H. In the first part of this study, bare Si wafers were spin-coated with a mixture of prehydrolyzed metal alkoxides [(3-glycidyloxypropyl-) trimethoxysilane and aluminum sec-butoxide, in

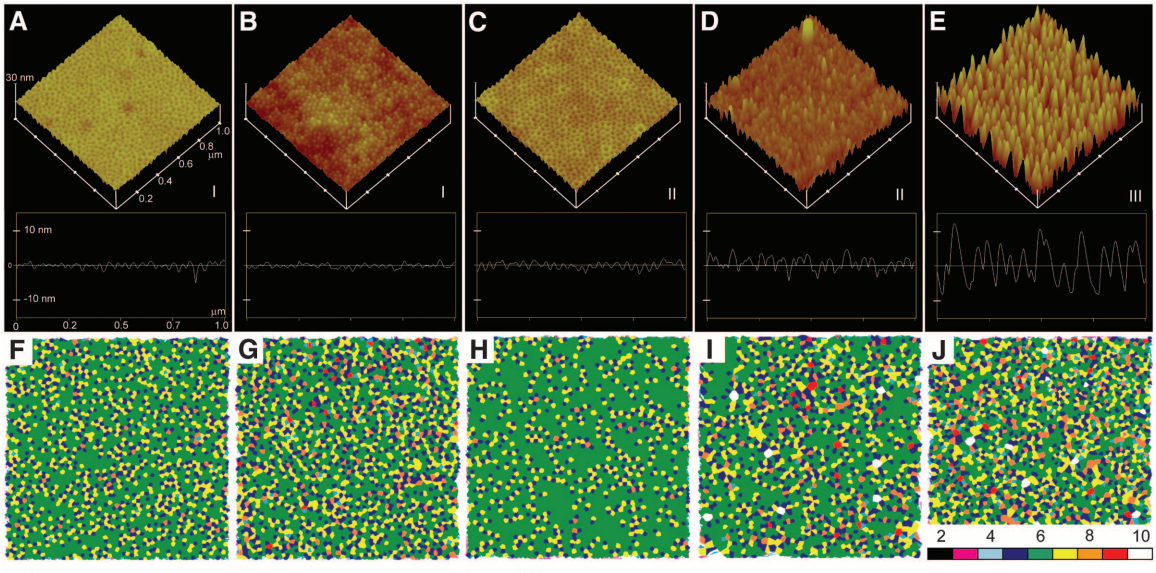

Fig. 2. AFM images with respective height profiles. (**A** and **C**) Porous templates. (**B**), (**D**), and (**E**) Si nanostructures. (**F** to **J**) Voronoi analysis of corresponding AFM images. (**K**) Table for samples s1 (I), s2 (II), and s3 (III). RDFs of (**L**) samples s1 and s3 and (**M**) sample s2 are shown. The scan size for all AFM images is 1×1 μm, and the scale bar (*y* axis) ranges from −15 to 15 nm in the height profiles. The scan area for Voronoi analysis is 2×2 μm^2.

K

Sample	Centers	Voronoi-6
Parent-I	3552	0.56
I	3226	0.45
Parent-II	3101	0.69
II	2759	0.53
Parent-III	4058	0.50
III	3142	0.39

a ratio of 8:2 by weight] and poly(isoprene-*b*-ethylene oxide) (PI-*b*-PEO) diblock copolymers (ratio of metal alkoxides to polymer, 6:1 by weight) in organic solvents (tetrahydrofuran:chloroform, 1:1 by weight) (*21*). Monolayers with inverse hexagonal nanostructure were formed (*22*), with one inorganic-rich domain (PEO + inorganic) and the other purely organic (PI). The organic components were subsequently removed by slow heating to 500°C, leaving an ordered nanoporous hexagonal array, with pores accessible from the top, Fig. 1A. For the block copolymers we used, the nanopore lattice spacings were between 30 and 35 nm, depending on the polymer molecular weight. The physical film thickness after calcination was 16 ± 1.6 nm, as determined by a combination of scanning electron microscopy (SEM) and x-ray diffraction (*22*). The nanopores were initially filled with Si through the use of 40-ns XeCl excimer pulsed laser irradiation [wavelength (λ) = 308 nm] (Fig. 1H). The template itself was transparent, with the laser light being absorbed by the Si substrate. Time-resolved reflectance (TRR) of the sample surface was monitored with a diode probe laser (λ = 650 nm) and was used to measure melt duration. At fluences (σ) above the melt threshold (~600 mJ/cm^2 for Si), the semiconducting solid became a metallic liquid, and the surface reflectance increased sharply (*23*), providing a fingerprint for understanding the mechanistic details of the process.

In first experiments, with sample s1, the porous template was irradiated with the excimer laser at fluences sufficient to melt the underlying Si substrate. Because of rapid cooling into the substrate, the total melt duration was only ~20 to 100 ns, and the total time at higher temperatures was less than a few microseconds, preventing sintering collapse of the porous silica-type template. After laser irradiation, the aluminosilicate template was dissolved away with a 48% hydrofluoric acid (HF) solution to expose the resulting array of Si nanopillars (Fig. 1, B and C). Figure 2, A and B, show atomic force microscopy (AFM) images of sample s1 before and after irradiation with five laser pulses of 40 ns duration and the subsequent removal of the skeletal aluminosilicate. The AFM results suggest excellent pattern transfer from the template into Si. The images were quantitatively analyzed with analysis tools described elsewhere (*24*, *25*). Figure 2, F and G, show representative Voronoi diagrams of the aluminosilicate template and the resulting nanostructured Si array, respectively. The Voronoi diagram represents the number of nearest neighbors of a pore or resulting Si nanostructure after melting and is color-coded to facilitate identification of defects and grain boundaries (*25*). The Voronoi-6 ratio, defined as the fraction of pores or resulting Si nanostructures with sixfold hexagonal nearest-neighbor symmetry, provides a simple metric for sample comparison. As indicated by the increased number of defects in the Voronoi diagram, the transformation from pores to Si nanopillars increases disorder in the system. However, transfer of the template into Si structures was accomplished with a high yield, with greater than 90% conversion of pores to Si nanopillars and only a 20% decrease in the Voronoi-6 ratio (Fig. 2K, sample s1).

Although in these experiments the transfer fidelity was high in the lateral dimensions, section analysis of AFM images showed the resulting Si nanostructures to be only 1 to 2 nm

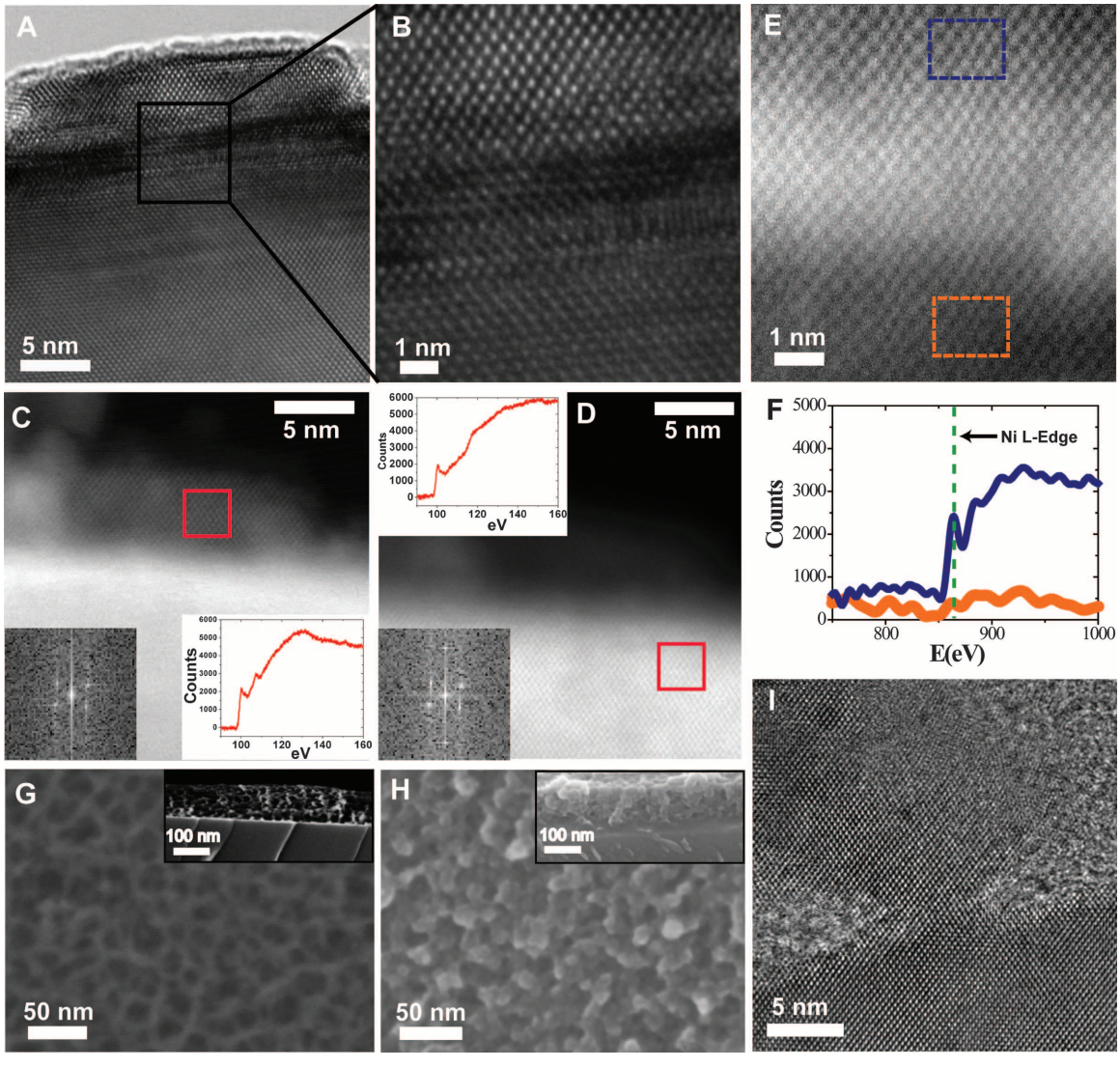

Fig. 3. EM images of homo- and heteroepitaxial nanostructures. (**A** and **B**) TEM images of Si nanostructure cross sections. The phase contrast reversals at the interface result from thickness changes in the sample: The substrate is thicker than the pillar, and the electrons undergo a larger phase shift in the substrate. STEM images, which do not suffer from contrast reversals with thickness, are shown for (**C**) nanostructure in focus and (**D**) Si substrate in focus. Corresponding EELS spectra and FFT insets are in (C) and (D). (**E**) STEM image of a NiSi pillar cross section on Si. (**F**) EELS spectra on the NiSi pillar and Si substrate from boxed regions in (E). (**G**) Top view and cross-sectional (inset) SEM images of the ~100-nm-thick porous niobia template. (**H**) Top view and cross-sectional (inset) SEM images of the porous Si nanostructure obtained from (G). (**I**) Cross-sectional TEM image of the thicker porous Si nanostructure in (H).

high (see height profile in Fig. 2B). This motivated the development of a second, modified, process in subsequent experiments, enabling better filling of the pores and thus forming taller Si nanopillars. To this end, an a-Si overlayer (Fig. 1, D to G) was deposited onto the template before laser irradiation. Furthermore, the native oxide present at the bottom of the pore was first removed by Ar ion sputtering before a-Si deposition in the same chamber and at the same base pressure. This resulted in a clean interface between deposited a-Si in the pore and the crystalline Si (c-Si) substrate (Fig. 1E). Laser irradiation at an energy density above the melt threshold of c-Si of sample films (sample s2) prepared in this way resulted in epitaxial crystallization of Si nanopillars from the substrate inside the pore (Fig. 1F). Subsequent HF (48%) treatment removed the oxide template, leaving behind an array of single-crystal nanopillars (Fig. 1G). The AFM image and Voronoi analysis (Fig. 2, C and D, and H and I, respectively) of the template and pillar array confirmed 89% pattern transfer and only a 23% decrease in the Voronoi-6 ratio (Fig. 2K, sample s2). The average height of pillars was found to be 6 to 7 nm, which is substantially higher than before (see height profile in Fig. 2D).

The epitaxial crystallinity of the Si nanopillars was confirmed by imaging pillar cross sections with high-resolution TEM and scanning TEM (STEM) (Fig. 3). The presence of lattice fringes in the pillars in congruence with the fringes in the substrate (Fig. 3, A and B) shows the crystalline nature of the nanopillars. The epitaxial growth of the nanopillars was confirmed by STEM-mode imaging, in which the Si substrate and nanopillar are both shown to be aligned along the [110] zone axis (Fig. 3, C and D). The two-dimensional fast Fourier transform (FFT) patterns on the pillar and substrate (lower left insets in Fig. 3, C and D, respectively) show that the two areas share the [111] reflections. Because of an offset in depth that exceeded the depth of field of the microscope for 0.3-nm fringes, STEM-mode images were taken with only the pillar (Fig. 3C) and only the substrate (Fig. 3D) in focus. Electron energy-loss spectroscopy (EELS) on the pillars (lower right inset in Fig. 3C) revealed the presence of a crystalline Si *L*-edge peak at 100 eV, also seen in the spectrum of the c-Si substrate (upper left inset in Fig. 3D). The small peak at 108 eV (inset of Fig. 3C) arises from Si in the thin SiO_2 surface layer that forms in air after HF treatment.

Because nanopores generated through block copolymer self-assembly laterally confine the crystal growth to narrow dimensions, it is possible to heteroepitaxially grow crystals with moderate lattice mismatch on Si. In this way, single-crystal nanostructures can be generated that are not easily accessible through etching. To this end, stoichiometric NiSi was sputter-deposited on the porous template (deposition rates were monitored with a crystal monitor) after the native oxide was removed. The NiSi (202) lattice mismatch to Si (220) was 0.5 to 0.6%, and in the absence of lateral confinement, NiSi film deposition on Si leads to multiple lattice orientations (*26*) and small-island formation, releasing the strain accumulated over larger lateral film distances. The nanoporous NiSi-filled films were then laser-irradiated to melt the amorphous NiSi, which subsequently solidified epitaxially from the substrate (*27*). The short duration of the melt minimized Ni diffusion or the incorporation of Si from the substrate into the liquid phase, thus maintaining the correct stoichiometry in the pore. The epitaxial orientation of the strained NiSi lattice on the c-Si substrate was confirmed by STEM images of the NiSi/Si interface, with the substrate aligned along the [110] zone axis (Fig. 3E). The EELS spectra collected on the pillar and the substrate clearly indicated the presence of a Ni *L*-edge peak on the pillar and an absence of Ni below the interface (Fig. 3F). The pore sizes generated through block copolymer self-assembly thus provided the necessary confinement for heteroepitaxy growth on single-crystal substrates for materials with moderate lattice mismatch.

We next examined the mechanistic aspects of the single-crystal nanopillar formation. A series of experiments was first performed (sample s3) in which the a-Si was deposited without etching the native oxide layer, thereby preventing direct growth from a c-Si substrate. The native oxide layer is expected to prevent molten Si from flowing through the pores, and hence deposited Si should remain confined to the pores (or on top of the template) when melted by the excimer laser pulse. This in turn should result in Si nanopillars of maximum height (~15 nm). This was indeed observed (see the AFM analysis in Fig. 2E). Voronoi analysis of AFM data revealed a 77% pore-to-pillar conversion, with a 22% decrease in the Voronoi-6 ratio (Fig. 2, J and K, sample s3).

For further quantitative data analysis, the radial distribution functions (RDFs) of the AFM images were computed for the parent templates and the resulting Si pillar nanostructures (Fig. 2, L and M). The RDFs of the unirradiated, parent templates exhibited narrow first-order maxima and multiple higher-order peaks. With no deposited films (sample s1), after irradiation the RDF

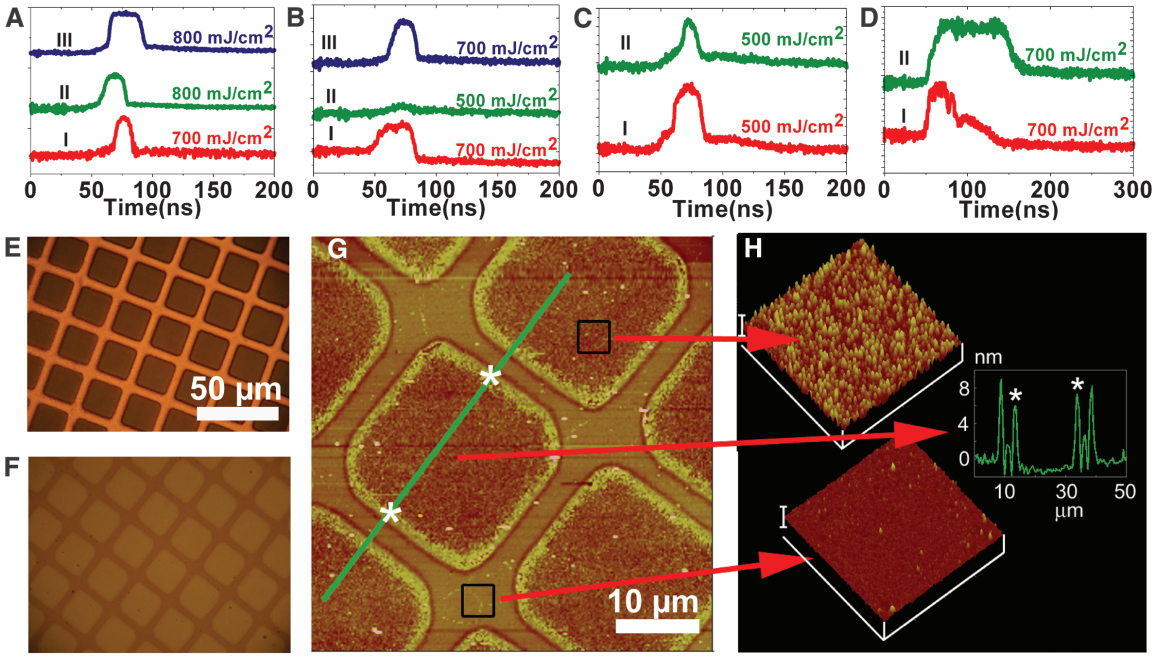

Fig. 4. Elucidation of the formation mechanism of single-crystal nanostructures. (**A**) TRR signal on (I) bare Si at 700 mJ/cm^2, (II) bare Si at 800 mJ/cm^2, and (III) sample s1 at 800 mJ/cm^2. (**B**) a-Si deposited on bare Si (I), first irradiation at 700 mJ/cm^2; (II) second irradiation at 500 mJ/cm^2 after (I); (III) second irradiation at 700 mJ/cm^2 after (I). (**C**) a-Si deposited on bare Si (I), first irradiation at 500 mJ/cm^2; (II) second irradiation at 500 mJ/cm^2 after (I). (**D**) Sample s2 (I), first irradiation at 700 mJ/cm^2; (II) second irradiation at 700 mJ/cm^2 after (I). Optical micrograph (**E**) of a copper TEM grid and (**F**) the resultant pattern on sample s3 (with deposited amorphous Si over the template) after laser exposure. (**G** and **H**) AFM images after HF treatment. Scan size is 2 × 2 μm, and the I bar along the *z* axis is 40 nm in (H).

exhibited very similar characteristics, with only slightly less power in each peak because of the slightly reduced ordering. In contrast, samples with deposited films where native oxide was not removed behaved quite differently (sample s3). The RDF of the resulting Si nanopillars exhibited a first-order maximum shifted to larger distances [pillar-to-pillar distance (r) = 39 nm] as compared to the template (r = 31 nm) and a rapid decay with no additional higher-order peaks. Examination of the AFM image in detail revealed sequences of pillars with the expected nearest-neighbor distance (r = 31 nm), surrounded by neighbors with distances closer to the expected second–nearest-neighbor value. This suggests that a substantial number of pores simply did not get filled, which is consistent with the 37% loss of centers from the Voronoi analysis. The corresponding RDF maximum indeed lies in between the nearest- and second–nearest-neighbor spacings and may be caused by a slight deformation of the template toward the empty space during melting.

The Si transient melt behavior during laser irradiation was monitored with TRR of samples. When irradiated above the melt threshold, the reflectance of a bare c-Si substrate will jump as the melt first forms, remain constant while the melt front propagates into the substrate, and decrease abruptly only as the surface solidifies (Fig. 4A, I). Increasing the fluence from 700 to 800 mJ/cm^2 extends the melt duration (that is, there is a broader reflectance curve) (Fig. 4A, II). Small changes in the reflectance before melting result from simple surface heating (*28*). We investigated three sample structures: (i) the c-Si substrate with the porous template, (ii) the c-Si substrate with a-Si on top, and (iii) the c-Si substrate with the template and a-Si deposited on top. With just the porous template (case i), the TRR signal remained very similar to that of the bare c-Si substrate, although the melt duration increased by ~8 ns at 800 mJ/cm^2 (compare traces in Fig. 4A, II and III). On the time scale of the laser pulse and melt duration, the cross-linked silica-type template does not undergo any substantial structural change. The extended melt duration arises partially from the antireflective nature of the porous template coating (*29*), but also suggests the incorporation of a low concentration of impurities (possibly O or Al) during solidification.

In case ii, with a-Si deposited directly on the c-Si substrate, the TRR signal strongly depended on the fluence (Fig. 4, B and C). With a lower melting temperature, the melt threshold for a-Si is less than that of c-Si (*30*). Epitaxial solidification can occur only for fluences sufficient to melt into the c-Si substrate (Fig. 4B), with polycrystalline Si (poly-Si) resulting at lower fluences (Fig. 4C) (*31*). Transformation of the a-Si could be readily confirmed visually (Fig. 1I). After irradiation at or above 700 mJ/cm^2, samples behaved similar to the bare substrate, with a melt threshold near 600 mJ/cm^2 (Fig. 4B, I to III). However, for initial irradiations below the melt threshold for c-Si (e.g., at 500 mJ/cm^2), a peak was observed in the TRR signal (Fig. 4C, I). When the spot was irradiated again at this fluence, the peak remained (Fig. 4C, II), indicating the formation of poly-Si structure with lower thermal conductivity.

From these results we concluded that in order to epitaxially crystallize a-Si deposited in the template pores (case iii), samples had to be irradiated above the melt threshold of c-Si. Upon irradiation (Fig. 4D, I), the reflectance first increased rapidly, then stayed constant, followed by a steep first drop; and finally further decreased gradually over several tens of nanoseconds. The drop in reflectance in two steps is probably due to the different time scales involved for heat transfer from molten Si to the substrate within a pore (faster) and at the top of the template, which is a poor heat conductor (slower). During a second irradiation at the same spot (Fig. 4D, II), the reflectance signal exhibited a single peak and decay, suggesting the absence of Si on top of the template. Because in various experiments more a-Si was deposited than was necessary to fill the pores, we speculate that this could only happen if the deposited Si on top of the template flowed through the pores to move under the template, displacing the template upward. The poor wetting properties (*32*) between molten Si and the aluminosilicate template might propel this surface tension–driven flow of molten Si through the template.

A key step in obtaining single-crystal epitaxy is to remove the native oxide layer to generate a clean interface between deposited amorphous material in a pore and the c-Si substrate. Maintaining this condition should enable the generation of single-crystal epitaxial nanostructures from thicker self-assembled porous templates. Argon ion sputtering removes oxide layers in direct line of sight from the top only. One challenge in working with silica-type structures is the need to remove the native oxide to enable the epitaxial crystallization, while not simultaneously removing the template. In order to work with thicker and more complex-shaped structures, we moved to a porous amorphous niobia template coupled with plasma-enhanced chemical vapor deposition (PECVD) to fill the porous structures with amorphous inorganic material. Figure 3G shows SEM images of a roughly 100-nm-thick porous amorphous niobia template with network structure. These templates were generated in a similar way as the aluminosilicate templates, using a poly(isoprene-*b*-styrene-*b*-ethylene oxide) (PI-*b*-PS-*b*-PEO, ISO) triblock copolymer with a molecular mass of 23,180 g/mol [17.2 volume % (vol %) PEO, 52 vol % PS; polydispersity index = 1.11] as structure-directing agent for a niobia sol as described elsewhere (*33*). The O + oxide volume fraction in the as-made composite was 24%. After spin coating, composite thin films heat-treated to 130°C (*33*) were plasma-cleaned to remove the organics, resulting in the desired porous nanostructure. The nanopore lattice spacing as revealed by SEM data was 32.5 ± 8.5 nm; that is, similar to that of the aluminosilicate templates. Figure 3H displays SEM images of the resulting porous Si nanostructures after removal of the native oxide with dilute HF, a-Si deposition, laser irradiation with two 40-ns laser pulses of 700 mJ/cm^2, and niobia template removal with concentrated HF (*21*). The images show that the Si has filled the pores, retaining the ~100-nm-thick template nanostructure. Cross-sectional TEM was performed on this sample to examine the epitaxial relationship between the silicon nanostructure and the substrate. In Fig. 3I, the Si lattice fringes in the porous nanostructure were found to be congruent with the fringes observed in the substrate, confirming the epitaxial correlation also for these thicker films (compare Fig. 3, A and I). Results of TEM imaging after plan-view polishing and electron diffraction on this sample are shown in fig. S1. Removing the native oxide layer before laser annealing indeed turned out to be a critical step. Fig. S2 shows two cross-sectional images of films etched for different times. When the native oxide was not removed completely (a 20-s etch), the crystal orientation in the film was independent of the substrate orientation and poly-Si formed. Extending the etch to 35 s resulted in single-crystal epitaxy in some regions of the film. In those regions where epitaxy had failed, the thin native oxide layer was still present. To go beyond the laboratory-scale proof of concept presented here, the oxide etchant needs to be able to penetrate small pores more reliably. This can be done with modern gas-phase semiconductor processing technology (with gaseous HF rather than liquid).

Finally, our bottom-up fabrication of epitaxially grown inorganic nanostructures was combined with top-down lithographic approaches to define specific areas, thus providing access to hierarchical nanostructures. As a proof-of-principle experiment, a TEM grid was used as a simple mask during the laser irradiation process to form patterns on a micrometer scale (Fig. 4E). The grid was placed in contact with the sample surface to minimize the loss of fidelity from the divergence of the homogenized incident laser beam (see fig. S3 for a schematic of the laser setup). The resulting Si pattern after irradiation through the TEM grid (Fig. 4F) indicates remarkable transfer. After template removal by HF, subsequent AFM imaging shows distinct squares of patterned material (Fig. 4G). Close-up images (Fig. 4H) of the square confirm the presence of Si nanostructures in the irradiated area and smooth flat Si in areas under the mask. As the image in Fig. 4G suggests and the AFM cross-sectional analysis confirms (Fig. 4H), the pattern edges of the irradiated areas are markedly higher than the interior of the areas. Despite poorly controlled edge effects, this simple proof-of-principle experiment does demonstrate that the placement of epitaxial single-crystal nanostructures can be controlled through simple imaging methods. Arbitrarily complex shapes should thus be possible to create by leveraging the wealth of patterning techniques currently available.

References and Notes

1. T. Yanagisawa, T. Shimizu, K. Kuroda, C. Kato, *Bull. Chem. Soc. Jpn.* **63**, 988 (1990).
2. C. T. Kresge, M. E. Leonowicz, W. J. Roth, J. C. Vartuli, J. S. Beck, *Nature* **359**, 710 (1992).

3. M. Templin *et al.*, *Science* **278**, 1795 (1997).
4. D. Zhao *et al.*, *Science* **279**, 548 (1998).
5. P. Yang, D. Zhao, D. I. Margolese, B. F. Chmelka, G. D. Stucky, *Nature* **396**, 152 (1998).
6. S. H. Joo *et al.*, *Nature* **412**, 169 (2001).
7. S. C. Warren *et al.*, *Science* **320**, 1748 (2008).
8. A. W. Vere, *Crystal Growth: Principles and Progress* (Plenum, New York, 1987).
9. J. Aizenberg, D. A. Muller, J. L. Grazul, D. R. Hamann, *Science* **299**, 1205 (2003).
10. M. Park, C. Harrison, P. M. Chaikin, R. A. Register, D. H. Adamson, *Science* **276**, 1401 (1997).
11. R. Ruiz *et al.*, *Science* **321**, 936 (2008).
12. C. Tang, E. M. Lennon, G. H. Fredrickson, E. J. Kramer, C. J. Hawker, *Science* **322**, 429 (2008).
13. T. Thurn-Albrecht *et al.*, *Science* **290**, 2126 (2000).
14. S. Y. Chou, C. Keimel, J. Gu, *Nature* **417**, 835 (2002).
15. C. De Rosa, C. Park, E. L. Thomas, B. Lotz, *Nature* **405**, 433 (2000).
16. P. Yang *et al.*, *Science* **282**, 2244 (1998).
17. B. Lee, T. Yamashita, D. Lu, J. N. Kondo, K. Domen, *Chem. Mater.* **14**, 867 (2002).
18. J. N. Kondo, K. Domen, *Chem. Mater.* **20**, 835 (2008).
19. A. S. Finnemore *et al.*, *Adv. Mater.* **21**, 3928 (2009).
20. E. S. Toberer, M. Grossman, T. Schladt, F. F. Lange, R. Seshadri, *Chem. Mater.* **19**, 4833 (2007).
21. See the supporting material on *Science* Online.
22. P. Du *et al.*, *Adv. Mater.* **16**, 953 (2004).
23. D. H. Auston, C. M. Surko, T. N. C. Venkatesan, R. E. Slusher, J. A. Golovchenko, *Appl. Phys. Lett.* **33**, 437 (1978).
24. A. Okabe, B. Boots, K. Sugihara, S. N. Chiu, *Spatial Tessellations: Concepts and Applications of Voronoi Diagrams* (Wiley, New York, 2000).
25. R. A. Segalman, A. Hexemer, R. C. Hayward, E. J. Kramer, *Macromolecules* **36**, 3272 (2003).
26. C. Detavernier *et al.*, *Nature* **426**, 641 (2003).
27. Thicker NiSi films with sufficient volume for x-ray diffraction confirm NiSi stoichiometry.
28. G. E. Jellison, D. H. Lowndes, D. N. Mashburn, R. F. Wood, *Phys. Rev. B* **34**, 2407 (1986).
29. G. E. Jellison Jr., D. H. Lowndes, J. W. Sharp, *J. Mater. Res.* **3**, 498 (1988).
30. J. M. Poate, J. Mayer, *Laser Annealing of Semiconductors* (Academic Press, New York, 1982).
31. M. O. Thompson *et al.*, *Phys. Rev. Lett.* **52**, 2360 (1984).
32. J. G. Li, H. Hausner, *Mater. Lett.* **14**, 329 (1992).
33. M. Stefik *et al.*, *Chem. Mater.* **21**, 5466 (2009).

34. The authors acknowledge financial support of this research by NSF through the Nanoscale Interdisciplinary Research Team program (grant DMR-0404195) and a creativity award to U.W. (grant DMR-0605856); the U.S. Department of Homeland Security (award no. 06-G-031); and the Energy Materials Center at Cornell (EMC^2), an Energy Frontiers Research Center funded by the U.S. Department of Energy Office of Science, Office of Basic Energy Sciences, under award no. SC0001086. K.W.T. gratefully acknowledges the Singapore Clean Energy Programme Office for a National Research Foundation graduate fellowship. The use of facilities of the Cornell Center for Materials Research, with funding from the Materials Research Science and Engineering Center program of NSF (under cooperative agreement DMR-0520404), and of the Cornell Nanoscale Science and Technology Facility, supported by NSF under grant no. ECS-0335765, is gratefully acknowledged. The authors also thank J. Gregoire, P. Huang, M. Thomas, S. Warren, C. Garcia, and R. Dorin for assistance in these experiments and A. Burns for help with graphics. A provisional patent application titled "Method for Large Mismatch Heteroepitaxy on Silicon" has been filed with Cornell University.

Supporting Online Material

www.sciencemag.org/cgi/content/full/330/6001/214/DC1
Materials and Methods
Figs. S1 to S3
References

7 June 2010; accepted 30 August 2010
10.1126/science.1193369

An Oxidative Enzyme Boosting the Enzymatic Conversion of Recalcitrant Polysaccharides

Gustav Vaaje-Kolstad, Bjørge Westereng, Svein J. Horn, Zhanliang Liu, Hong Zhai, Morten Sørlie, Vincent G. H. Eijsink*

Efficient enzymatic conversion of crystalline polysaccharides is crucial for an economically and environmentally sustainable bioeconomy but remains unfavorably inefficient. We describe an enzyme that acts on the surface of crystalline chitin, where it introduces chain breaks and generates oxidized chain ends, thus promoting further degradation by chitinases. This enzymatic activity was discovered and further characterized by using mass spectrometry and chromatographic separation methods to detect oxidized products generated in the absence or presence of $H_2{}^{18}O$ or $^{18}O_2$. There are strong indications that similar enzymes exist that work on cellulose. Our findings not only demonstrate the existence of a hitherto unknown enzyme activity but also provide new avenues toward more efficient enzymatic conversion of biomass.

The transition to a more environment-friendly economy has spurred research on enzymes capable of efficiently degrading recalcitrant polysaccharides, such as cellulose and chitin (Fig. 1A), for the production of biofuels (*1*). Traditionally, enzyme systems capable of degrading such polysaccharides are considered to consist of endo-acting enzymes that cut randomly in the polysaccharide chain and processive exo-acting enzymes (chito- or cellobiohydrolases), which degrade the polymers from chain ends. All these enzymes are hydrolytic and are referred to as glycoside hydrolases. Although this model is generally accepted, it remains difficult to understand how the glycoside hydrolases could act on a polysaccharide chain in its crystalline environment, and biochemists have speculated about the existence of a substrate-disrupting factor that could make the crystalline substrate more accessible to hydrolytic enzymes (*2*).

Recently, it was discovered that microorganisms that break down chitin, a crystalline analog of cellulose occurring in the shells of insects and crustaceans, indeed produce a protein that increases substrate accessibility and potentiates hydrolytic enzymes (*3*) (Fig. 1B). These proteins are classified as carbohydrate-binding modules (CBMs) and belong to family CBM33 as defined in the Carbohydrate Active Enzymes (CAZy) database (*4*, *5*). The first example of such a protein is CBP21 (CBP for chitin-binding protein), produced by the chitinolytic bacterium *Serratia marcescens*. As another example, two CBM33-containing proteins from *Thermobifida fusca* potentiate chitin hydrolysis by chitinases and cellulose hydrolysis by cellulases (*6*). Genes putatively encoding CBP21-like proteins are abundant in bacteria and viruses but are rare in eukaryotes. Fungi produce proteins classified as family 61 glycoside hydrolases (GH61) that act synergistically with cellulases (*7*) and are structurally similar to CBM33 proteins (*7*, *8*) (Fig. 1, B and C). The structural similarity includes a diagnostic conserved arrangement of the N-terminal amino group and two histidines that bind a metal ion (Fig. 1D). One of these histidines (His^{28}/His^{19} in Fig. 1D) is the N-terminal residue of the mature protein that results after proteolytic processing of the signal peptide during secretion. So far, the mechanisms employed by CBP21-like and GH61-like proteins have remained elusive.

We show here that CBP21 is an enzyme that catalyzes cleavage of glycosidic bonds in crystalline chitin, thus opening up the inaccessible polysaccharide material for hydrolysis by normal glycoside hydrolases. This enzymatic activity was first discovered when we detected traces of previously unidentified chitooligosaccharides upon incubation of β-chitin nanowhiskers with CBP21 (Fig. 2A) (*9*). The products were identified as chitin oligosaccharides with a normal sugar at the nonreducing end and an oxidized sugar, 2-(acetylamino)-2-deoxy-D-gluconic acid (GlcNAcA), at the other end (Fig. 2B and fig. S1). Addition of reductants dramatically increased the efficiency of the reaction (Fig. 2, C and D), which enabled the breakdown of large crystalline β-chitin particles by CBP21 alone (Fig. 2), with the release of a range of oxidized products (figs. S2 and S3 and below). In the presence of a reductant such as ascorbic acid, CBP21 boosted chitinase efficiency to much higher levels than previously observed (Fig. 2D) (*3*). Biotechnological applications could take advantage of the ability to increase CBP21 activity by adjusting the reaction conditions.

If CBP21 acts randomly on crystalline surfaces, one would expect generation of longer

Department of Chemistry, Biotechnology and Food Science, Norwegian University of Life Sciences, Post Office Box 5003, 1432 Ås, Norway.

*To whom correspondence should be addressed. E-mail: vincent.eijsink@umb.no